

# Large Area Honeycomb-Structured TiO<sub>2</sub> Film for Photocatalytic Water Splitting

Myeongseok Jang,<sup>†</sup> Hyunjung Lee,<sup>‡</sup> and Wonmok Lee\*<sup>†</sup>

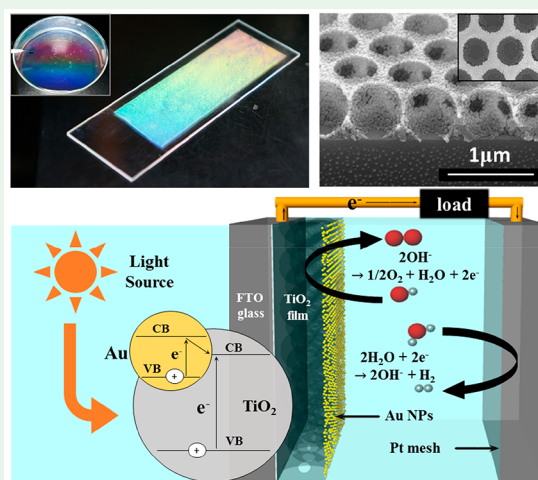
<sup>†</sup>Department of Chemistry, Sejong University, 209 Neungdong-ro, Gwangjin-gu, Seoul 05006, Korea

<sup>‡</sup>School of Advanced Materials Engineering, Kookmin University, 861-1 Jeongneung-dong, Seoul 136-702, Korea

## Supporting Information

**ABSTRACT:** We demonstrate the fabrication of a large area 2-dimensional (2-D) binary colloidal assembly of polymeric microspheres ( $\mu$ -spheres) and TiO<sub>2</sub> nanoparticles (NPs). TiO<sub>2</sub> NPs near the surface of poly(methyl methacrylate) (PMMA)  $\mu$ -spheres in aqueous dispersion exerted attractive depletion force between  $\mu$ -spheres, allowing the formation of the well-ordered composite monolayer having hexagonal close-packed (hcp) structure on the air–water interface which can be transferred to a solid substrate. Subsequent drying and calcination of the composite film resulted in an “egg plate” structured TiO<sub>2</sub> film. When additional TiO<sub>2</sub> dispersion was spin-coated on the composite monolayer, an interesting honeycomb structured TiO<sub>2</sub> film was obtained. After the photodeposition of Au NPs on the honeycomb structured TiO<sub>2</sub> film for an enhanced absorptivity of visible light, the film was tested as a photoelectrode for photocatalytic water splitting. Owing to the large surface area of the well-ordered 2-D porous structure, a photoanode with the honeycomb-structured TiO<sub>2</sub> thin film exhibited a 67 times higher photocurrent density (PCD) for water splitting compared to the value from nanoporous TiO<sub>2</sub> photoanode with the same thickness.

**KEYWORDS:** colloidal self-assembly, air–water interface, opal monolayer, honeycomb structure, depletion force, photocatalytic water splitting



## 1. INTRODUCTION

Colloidal self-assembly has been studied extensively as it is a facile method for fabricating the scaffold structure of various functional materials while providing multiple advantages such as simplicity of fabrication process, cost-effectiveness, and diverse structural dimensionality.<sup>1</sup> For instance, colloidal arrays can be fabricated in one-dimensional (1-D) linear arrays;<sup>2</sup> further, two-dimensional (2-D) colloidal monolayers on planar substrates have been fabricated.<sup>3</sup> Three-dimensional (3-D) colloidal crystals are often called “artificial opals” as their structure resembles that of naturally occurring opal gemstones.<sup>4</sup> Among dimensional diversities, 2-D colloidal arrays can be applied as photomasks, superhydrophobic coating, sensors, and so on<sup>5</sup> by providing template structures for the functional materials to be infiltrated within their interstitial spaces. For example, the composite arrays of colloidal microspheres ( $\mu$ -spheres) and hydrogels were used as colorimetric chemical sensors.<sup>5</sup> If the volume of the hydrogel is changed by an external field, it can be used as a reflective display.<sup>6</sup> Another application of the composite colloidal array is a photocatalyst having TiO<sub>2</sub> nanoparticles (NPs) within a colloidal assembly.<sup>7</sup> The fabrication of the composite colloidal array can be categorized as follows: (1) two-step process of colloidal assembly and postinfiltration of functional materials

and (2) one-step assembly of colloidal template and functional materials. The 2-D binary colloidal assembly has been demonstrated by spin-coating a mixed dispersion of organic and inorganic  $\mu$ -spheres in water/alcohol media.<sup>8</sup> Recently, two different-sized polymer  $\mu$ -spheres were reported to form close-packed monolayers on an air–water interface in the presence of ionic surfactants.<sup>9</sup> It is reported that the colloidal monolayer can be transferred from the air–water interface to a glass substrate that had been immersed in water by draining water out from a Langmuir–Blodgett trough.<sup>10</sup> The capillary effect has been utilized to easily transfer self-assembled 2-D composite films from an air–water interface to a substrate.<sup>11</sup> It was shown that the various chemical sensors can be fabricated by using 2-D colloidal crystals comprising hydrogels containing binding sites for specific analytes.<sup>5</sup> Unlike a 3-D opal film, a 2-D photonic crystal does not require light penetration for diffraction, and material consumption can be minimized. The transfer of a colloidal monolayer from an air–water interface onto a solid substrate allows almost no material loss while a substantial amount of colloidal materials is wasted in dip-

**Received:** September 20, 2019

**Accepted:** November 5, 2019

**Published:** November 19, 2019

coating and spin-coating methods. Functional materials can be incorporated within a 2-D opal template either by the postinfiltration method<sup>5</sup> or by the simultaneous assembly of different materials. From the viewpoint of simplicity, simultaneous fabrication of binary colloids on an air–water interface would be more desirable. In this study, we investigate a single-step fabrication of a hybrid monolayer of close-packed  $\mu$ -spheres and TiO<sub>2</sub> nanocrystals on an air–water interface followed by a transfer to a solid substrate. The 2-D structured TiO<sub>2</sub> film on a transparent electrode is tested as an electrode for photocatalytic water splitting.

## 2. EXPERIMENTAL SECTION

**Synthesis of Monodispersed PMMA  $\mu$ -Spheres.** Monodispersed poly(methyl methacrylate) (PMMA)  $\mu$ -spheres were synthesized by emulsion polymerization,<sup>12</sup> in which 18 mL of DI water in a reactor of 50 mL three-neck flask was degassed by using N<sub>2</sub> gas for 30 min. Subsequently, a 2 mL aliquot of degassed water was removed, in which 0.0598 g of potassium persulfate (PPS, 99.99%, Sigma-Aldrich) was dissolved. After the temperature of reactor was elevated to 90 °C, PPS and 8.0025 g of methyl methacrylate (MMA, Sigma-Aldrich) were injected. The reaction proceeded for 1.5 h. The resulting milky product was purified by centrifugation at 6000 rpm (LaboGene) thrice and stored in a refrigerator in the presence of an ion-exchange resin. The particle size and zeta potential were characterized by using a dynamic light scattering apparatus (Zetasizer Nano ZS, Malvern).

**Synthesis of Charge-Stabilized TiO<sub>2</sub> Nanoparticle.** Anatase TiO<sub>2</sub> NPs were synthesized by the following procedure.<sup>13</sup> Deionized (DI) water (108 mL) in a 250 mL flask was stirred vigorously with a magnetic bar, where 6 mL of titanium(IV) isopropoxide (97%, Sigma-Aldrich) was added dropwise and left for 1 h for sol–gel reaction to occur. The resulting crude product was washed by centrifugation (2000 rpm, 10 min) thrice, and finally 30 mL of DI water was added. Pulsed mode ultrasonication was performed for 5 min (S-4000, Misonix). The product was subsequently transferred to a 100 mL flask, in which 2 mL of tetramethylammonium hydroxide (25% in water, Sigma-Aldrich) was added, and peptization was performed at 85 °C for 24 h under vigorous agitation. The translucent product was transferred to a 45 mL acid digestion vessel (model 4744, Parr) and stored in an oven at 200 °C for 1 h. The product was washed by centrifugation at 15000 rpm and diluted with DI water. The dried product was characterized by using an X-ray diffractometer (D/MAX-2500, Rigaku).

**Fabrication of PMMA/TiO<sub>2</sub> Composite Thin Film and TiO<sub>2</sub> Inverse Opal Film.** Aqueous dispersions of PMMA  $\mu$ -spheres and TiO<sub>2</sub> NPs were mixed at the same mass ratio, and the same volume of ethanol was added to obtain a 1 wt % suspension. The binary dispersion was filled in a 1 mL syringe (Kovax) and spread on the air–water interface by using a syringe pump at 4 mL/h with the needle tip (25G 5/8 in.) barely touching the water surface. Upon the formation of the PMMA/TiO<sub>2</sub> composite monolayer, rainbow-colored diffraction was observed. Prior to sample spreading, a slide glass (or FTO) was immersed in water, on which the composite monolayer film was transferred by gently scooping up with a tweezers. After drying at ambient air, the PMMA/TiO<sub>2</sub> composite thin film was affixed on glass. After annealing at 90 °C, the film was calcined at 500 °C to yield a TiO<sub>2</sub> inverse opal thin film. The film was characterized by using a field emission scanning electron microscope (FE-SEM, S-4700, HITACHI) and energy dispersive X-ray spectrometer (ED-XS, HORIBA).

**Photodeposition of Au NP.** An aqueous 0.01 M sodium chloroaurate dehydrate (NaAuCl<sub>4</sub>·2H<sub>2</sub>O, Sigma-Aldrich) solution was prepared in a 50 mL vial and was stored in a refrigerator. For the photodeposition of Au, 42 mL of methanol and 8 mL of Au precursor were mixed in a custom-made quartz cell (40 mm × 50 mm × 80 mm). A TiO<sub>2</sub> inverse opal film on FTO was immersed in quartz cell, and UV light (HgXe lamp, EXECURE 400, 200 W) was exposed for 8 min to induce photodeposition.

**Diffraction Measurements of 2-D Photonic Films.** The 2-D reflectance of photonic crystal arrays with lattice parameter 500–600 nm was measured by using a light source (Halogen display/optic lamp, OSRAM) and a UV–vis spectrometer (Avaspec, Avantes) equipped with an optic cable and a collimator (Avantes) with angles of incidence and detection of 46° and –20°, respectively, to the normal plane. A diffraction grating with 1200 grooves/mm (Edmund Optics) was used for reference.

**PEC Water Splitting.** For the PEC water-splitting experiment, three electrode cells were fabricated. In a custom-made quartz cell (40 mm × 50 mm × 80 mm), an Au/TiO<sub>2</sub> inverse opal thin film on FTO was used as the operating electrode, and Pt mesh (1 in. × 1 in.) and Ag/AgCl (3 M NaCl, WonATech.) were used as a counter electrode and reference electrode, respectively. Additionally, 70 mL of 1.0 M KOH aqueous solution was used for one PEC water-splitting experiment, and a 150 W Xe arc lamp (LS-150, Abet tech.) at AM 1.5 G (1 SUN) was used as a light source. By use of a potentiostat (CompactStat, IVIUM), 0.217 V vs Ag/AgCl was applied, corresponding to 1.23 V vs the reference hydrogen electrode (RHE).<sup>14</sup> The photocurrent density (PCD) was measured by using a potentiostat (Compactast, IVIUM) while switching the Xe lamp on and off every 1 min. To examine the PEC efficiency of the photoanode at the visible light wavelength, the measurements were performed with or without a long-pass filter (cutoff wavelength at 420 nm, Edmund Scientific).

## 3. RESULTS AND DISCUSSION

**Preparation and Characterization of TiO<sub>2</sub> NP, Poly(methyl methacrylate) (PMMA)  $\mu$ -Sphere, and Binary Dispersion.** Two different colloidal particles were synthesized to prepare a binary colloidal suspension in water. The emulsion-polymerized PMMA  $\mu$ -sphere was used as an opal-forming particle, and TiO<sub>2</sub> NPs were prepared by sol–gel synthesis and subsequent hydrothermal treatment. The measured average diameters ( $D_{av}$ ) of TiO<sub>2</sub> and PMMA by using SEM were 31 and 564 nm, respectively, as shown in Figures 1a,b and Table 1.

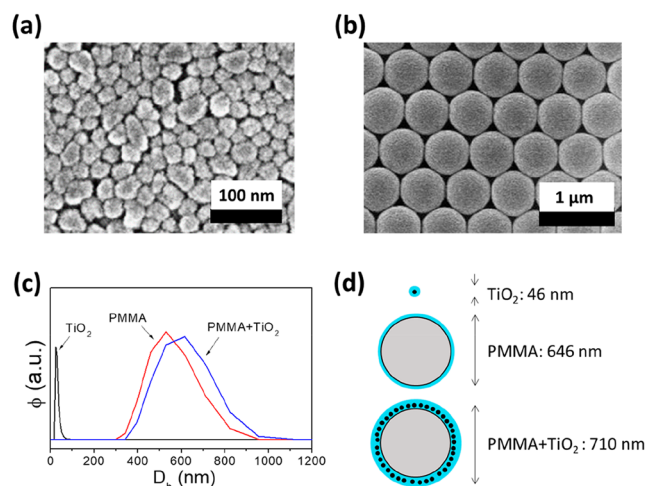


**Figure 1.** SEM images of (a) TiO<sub>2</sub> and (b) PMMA used in this study. (c) DLS measurements of hydrodynamic size ( $D_h$ ) distributions of the colloidal particles and (d) their schematic illustration.

Aqueous dispersions of TiO<sub>2</sub> NP, PMMA  $\mu$ -sphere, and their binary mixtures were prepared for dynamic light scattering (DLS) and zeta-potential ( $\zeta$ ) measurements (Supporting Information, Figure S1).

As shown in Table 1, the results indicate that all three dispersions exhibit negative surface potentials, and both TiO<sub>2</sub>

**Table 1. Averaged Size and Surface Charge Properties of the Particles and Their Mixture**

	TiO <sub>2</sub>	PMMA	PMMA + TiO <sub>2</sub>
$D_{av}$ (by SEM), nm	31 ± 8	564 ± 7	N.A.
$D_h$ (by DLS), nm	46.4 ± 1	646 ± 1	710 ± 8
$\xi$ , mV	-43 ± 4	-63 ± 6	-62 ± 7

and PMMA exhibit larger  $D_h$  values compared to  $D_{av}$  from SEM analysis as  $D_h$  indicates the Z-averaged Stokes diameter from DLS measurements that includes an electric double-layer thickness and surfactants, if present. As shown in Figure 1c and Table 1, the  $D_h$  of a PMMA/TiO<sub>2</sub> binary dispersion is 10% (~67 nm) larger than that of PMMA; this can be attributed to the TiO<sub>2</sub> NPs surrounding PMMA  $\mu$ -sphere, as depicted in Figure 1d. Lewis and co-workers reported a highly charged “nanoparticle halo” on a silica  $\mu$ -sphere that exerted a depletion attraction between  $\mu$ -spheres in an aqueous medium. Although our system differs in  $\mu$ -sphere by containing negative surface charges, DLS analysis indicates the contribution of TiO<sub>2</sub> NPs to an increased  $D_h$  of PMMA  $\mu$ -spheres in aqueous binary dispersion.

**Formation of Hexagonally Close-Packed Composite Monolayer Arrays of PMMA/TiO<sub>2</sub>.** Using the PMMA/TiO<sub>2</sub> binary dispersion, we fabricated a 2-D colloidal monolayer film on an air–water interface. Figure 2 schematically demonstrates the formation of 2-D photonic crystal films of PMMA/TiO<sub>2</sub> composite monolayer on an air–water interface and subsequent transfer onto a solid substrate.

As rationalized above, we assumed that the majority of TiO<sub>2</sub> NPs surrounded the surface of PMMA  $\mu$ -spheres. For an efficient formation of a colloidal monolayer, the aqueous

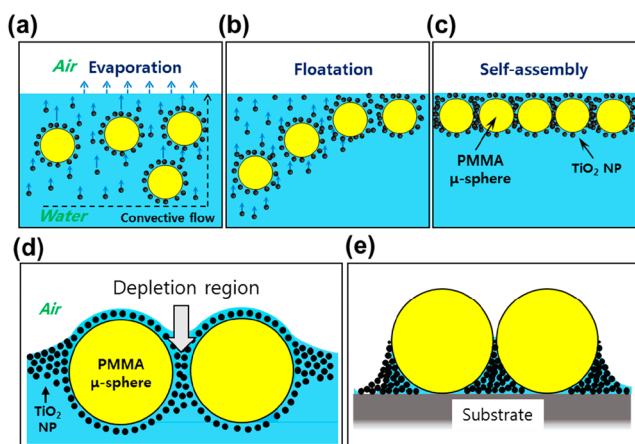


**Figure 2.** Schematic illustration of PMMA/TiO<sub>2</sub> composite monolayer formation on an air–water interface and subsequent transfer to a substrate. (a) As-injected PMMA  $\mu$ -spheres and TiO<sub>2</sub> NPs are immersed beneath the water surface while evaporation of volatile solvent (ethanol) causes enhanced upward convection of liquid. (b) With PMMA being surrounded by TiO<sub>2</sub> NPs, both particles are driven upward along with mass flow of liquid and remain at the air–water interface. (c) PMMA and TiO<sub>2</sub> particles are self-organized into an hcp structure on the air–water interface. (d) During the self-assembly of particles on air–water interface, the capillary force of water causes attractive force between adjacent PMMA  $\mu$ -spheres while smaller TiO<sub>2</sub> NPs are jammed between PMMA particles to exert osmosis-induced depletion force. (e) After transferring to a substrate and subsequent water evaporation, a 2-D PMMA/TiO<sub>2</sub> composite photonic crystal is formed.

dispersion was mixed with ethanol prior to spreading.<sup>15</sup> Once a binary dispersion was spread on the air–water interface, both the PMMA  $\mu$ -spheres and TiO<sub>2</sub> NPs experienced an upward convective force because of the rapid evaporation of ethanol, thus promoting the flotation of both colloids<sup>11</sup> (Figure 2a). Once-floated colloidal particles remained on the air–water interface due to strong surface tension<sup>16</sup> (Figure 2b,c). The curved meniscus of water on the  $\mu$ -spheres’ surface exerts a capillary force between the  $\mu$ -spheres to drive the close packing of  $\mu$ -spheres with a continuous supply of binary colloids<sup>5</sup> (Figure 2d). Despite the strong surface tension exerted to the  $\mu$ -spheres at the air–water interface, electrostatic repulsion between  $\mu$ -spheres prevents their physical contact due to surface charge, thereby maintaining some extent of interparticle distance even in the close-packed structure. However, as the PMMA  $\mu$ -spheres are close-packed with each other, TiO<sub>2</sub> NPs at the vicinity of two PMMA particles are entropically depleted to result in a further close-packing of PMMA  $\mu$ -spheres.<sup>17</sup> The balance between depletion attraction and electrostatic repulsion had shown to promote a hard-sphere-like behavior of colloidal dispersion in previous investigations, in which silica  $\mu$ -spheres and zirconia NPs were employed.<sup>18</sup> A “hard-sphere interaction” enables a closer interparticle distance without coagulation compared to a typical charge-stabilized system. In this study, the same analogy can be applied because negatively charged TiO<sub>2</sub> NPs<sup>19</sup> near a PMMA surface can exert depletion force between  $\mu$ -spheres, thus resulting in a shorter distance between the close-packed  $\mu$ -spheres at the air–water interface. Both PMMA and TiO<sub>2</sub> are negatively charged in water; thus, they are free from aggregation during the self-assembly process.<sup>19</sup> A previous investigation had indicated that the interparticle interaction between large spheres was stronger than that between small particles.<sup>20</sup> Owing to the strong interaction, large  $\mu$ -spheres will be assembled into the hcp structure, and the overall potential energy of the system is minimized with the small particles at the interstitial space called the “threefold void” between large  $\mu$ -spheres.<sup>21</sup> However, Bishop et al. did not account for the depletion interaction since the second particle was not small enough to exert depletion force. Because the average particle size of the TiO<sub>2</sub> NP used in this study is ~20 times smaller than that of the PMMA  $\mu$ -sphere, a depletion force could be realized. When the self-assembled PMMA/TiO<sub>2</sub> composite monolayer film at the air–water interface is transferred to a glass substrate, a subsequent water evaporation will cause the TiO<sub>2</sub> NPs to be swept down to the substrate surface; finally, a dried monolayer film of PMMA  $\mu$ -spheres will be formed with TiO<sub>2</sub> NPs uniformly packed within the 3-fold voids (Figure 2e). With regard to the monolayer formation, the PMMA  $\mu$ -spheres can self-assemble into an hcp monolayer on the air–water interface without TiO<sub>2</sub> NPs. However, TiO<sub>2</sub> dispersion without PMMA  $\mu$ -spheres did not form a stable monolayer on the air–water interface. A stable TiO<sub>2</sub>/PMMA composite monolayer on the air–water interface and unfavorable formation of a TiO<sub>2</sub>-only film again indicate the formation of a nanoparticle halo around PMMA  $\mu$ -spheres as discussed in Figure 1.

Photographs of the self-assembled monolayers of PMMA  $\mu$ -spheres without and with TiO<sub>2</sub> NPs on the air–water interface and on the glass substrate are shown in Figures 3a and 3b, respectively. Once the dispersion in the water/ethanol mixture is spread continuously onto the water surface, a rainbow color begins to appear, implying that the PMMA  $\mu$ -spheres have self-

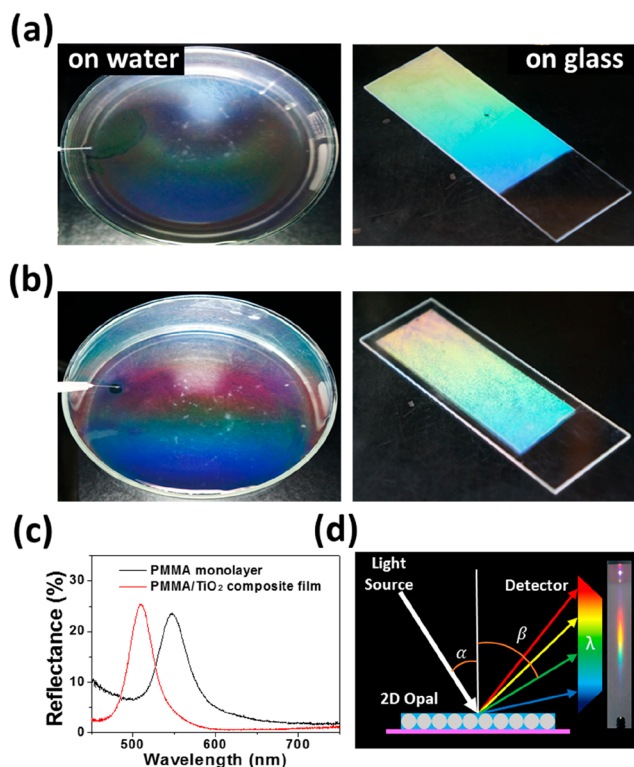


**Figure 3.** Photographs illustrating self-assembled monolayers of (a) PMMA and (b) PMMA/TiO<sub>2</sub> on the air–water interface (left) and on the glass slide (right). A needle tip is shown at the left corner of each glass dish from which colloidal suspension is being discharged. (c) Reflectance spectra of each film on glass substrate. The spectrum from a PMMA monolayer indicated  $R_{\max} = 22.9\%$  at  $\lambda_{\text{peak}} = 551$  nm, and that from a PMMA/TiO<sub>2</sub> composite film indicated  $R_{\max} = 25.5\%$  at  $\lambda_{\text{peak}} = 509$  nm. (d) Reflectance measurement for 2-D opal film. The incident angle ( $\alpha$ ) and detection angle ( $\beta$ ) were fixed at 46° and 60°, respectively.

assembled to a hexagonal close-packed (hcp) monolayer structure and light diffraction resulted in a rainbow color. A glass substrate (25 × 75 mm<sup>2</sup>) that had been immersed in water was gently lifted to scoop up the composite monolayer

film along with the water layer, and the subsequent evaporation of water at the ambient condition resulted in a dried monolayer without hcp structure disruption, as shown in Figures 3a,b. Compared to the upper images of monolayers from the  $\mu$ -spheres only, the composite monolayers of PMMA/TiO<sub>2</sub> exhibited stronger diffraction colors on both surfaces.

A stronger diffraction can be attributed to the presence of TiO<sub>2</sub> NPs that enhance the reflection of incident light because of a high index of refraction ( $n \sim 2.0$  at 400 nm).<sup>13</sup> The enhanced diffraction could be confirmed by measuring the 2-D reflectance spectrum that exhibits a peak, following the diffraction equation

$$m\lambda_{\text{peak}} = d(\sin \alpha \pm \sin \beta) \quad (1)$$

where  $m$  is the diffraction order,  $\lambda_{\text{peak}}$  is the wavelength of the reflectance peak,  $d$  is the distance between the  $\mu$ -spheres, and  $\alpha$  and  $\beta$  are angles of incidence and detection, respectively. The experimental setup for diffraction measurements is shown in Figure S2. As shown in Figure 3c, the reflectance peak from a PMMA/TiO<sub>2</sub> composite monolayer exhibited a higher peak intensity ( $I_{\max} = 25.5\%$  vs 22.9%) and a slightly narrower peak width (fwhm = 32.9 nm vs 38.0 nm) compared to that from a PMMA monolayer. For a precise comparison of reflectance measurement, the angles of incidence and detection were fixed at 46° and 60°, respectively, as shown in Figure 3d. It is noteworthy that  $\lambda_{\text{peak}}$  from a PMMA/TiO<sub>2</sub> composite monolayer was found at 509 nm, which is 42 nm shorter than that from a PMMA monolayer, indicating a shorter distance between the  $\mu$ -spheres for a composite monolayer. As discussed earlier, the existence of highly charged NPs in the vicinity of the  $\mu$ -spheres exerted a “depletion attraction” between the  $\mu$ -spheres, thus resulting in a decreased interparticle distance.<sup>17</sup> A shorter  $\lambda_{\text{peak}}$  observed from a PMMA/TiO<sub>2</sub> composite monolayer compared to that from a PMMA monolayer indicates that the transferred film maintains a shorter  $d$ .

Upon the complete drying and annealing of the composite monolayer film on a glass substrate (Figure 4a), it was calcined at 500 °C to yield an “egg plate” structure of TiO<sub>2</sub>, as schematically shown in Figure 4b. When an additional TiO<sub>2</sub>

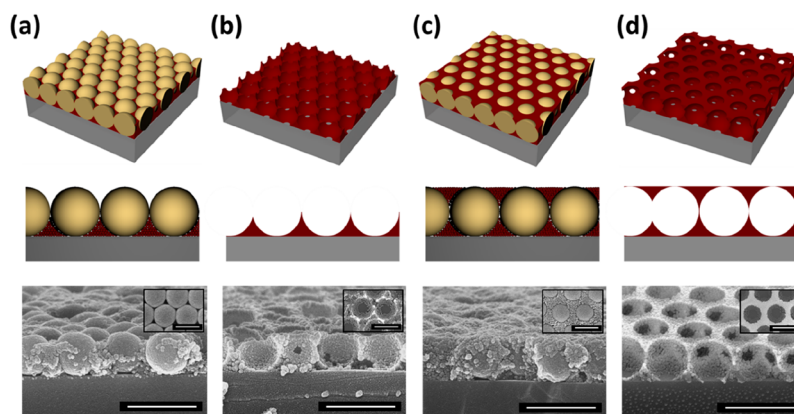


**Figure 4.** Schematic diagrams illustrating fabrication procedures of TiO<sub>2</sub> inverse opal thin film and SEM images of corresponding monolayer films. (a) PMMA/TiO<sub>2</sub> composite film is formed upon drying and annealing. (b) “Egg plate” structure is formed upon elimination of PMMA  $\mu$ -spheres from (a). (c) Addition of TiO<sub>2</sub> NPs onto a PMMA/TiO<sub>2</sub> composite film. (d) Elimination of PMMA  $\mu$ -spheres from (c) results in a “honeycomb” film structure. At the bottom are SEM images of composite opal films and inversed opal films on glass slides. Insets show top-view images of each film (scale bar: 1  $\mu\text{m}$ ).

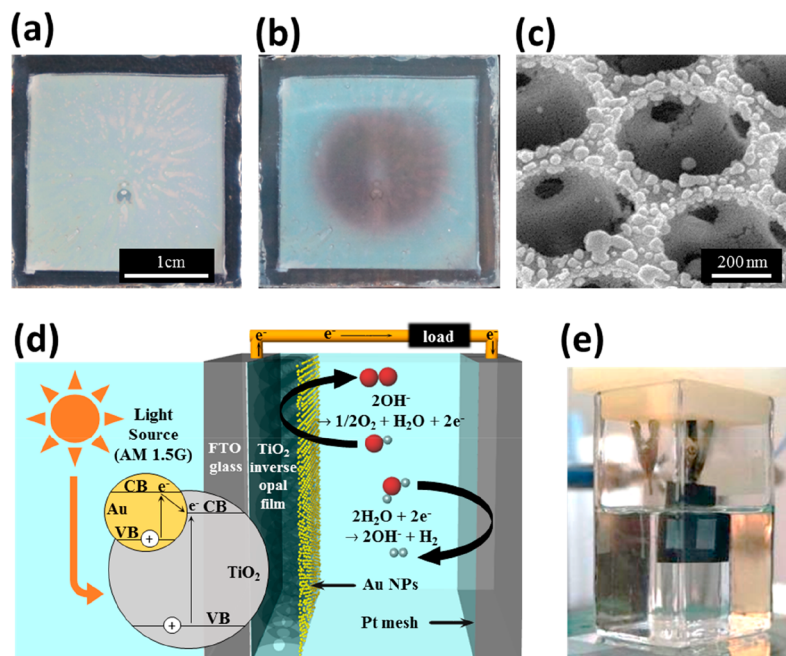


**Figure 5.** Honeycomb-structured  $\text{TiO}_2$  film on FTO after additional  $\text{TiO}_2$  spin coating and calcination (a) and after Au photodeposition (b). (c) SEM image showing Au NPs on  $\text{TiO}_2$  inverse opal surface. (d) Schematic illustration of PEC water splitting and (e) quartz cell equipped with three electrodes of  $\text{TiO}_2/\text{Au}$  photoanode, Pt mesh counter electrode, and Ag/AgCl reference electrode for the photoelectrochemical water-splitting experiment.

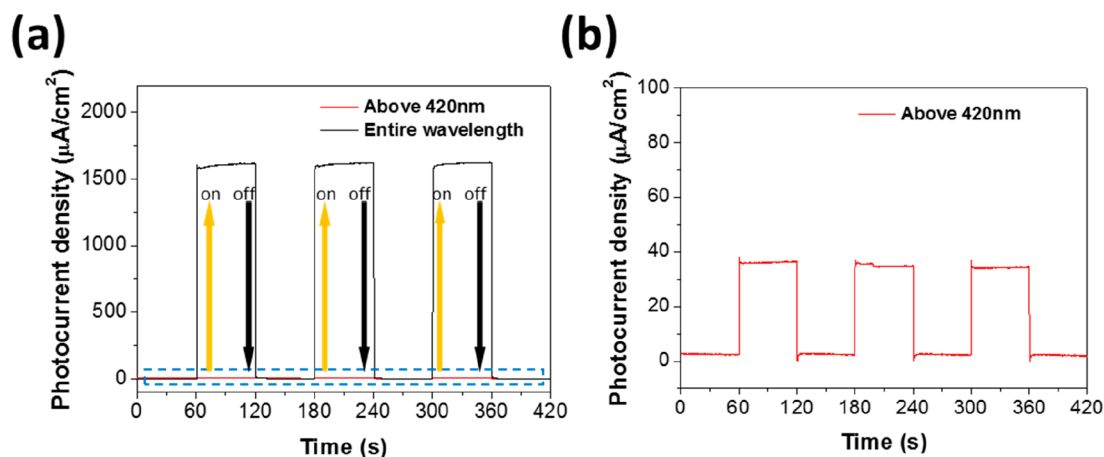


**Figure 6.** Photoelectrochemical performance of  $\text{TiO}_2$  inverse opal thin film with applied potential of 1.23 V vs RHE and illumination of all wavelength ranges of light (a) and visible light with wavelength  $\geq 420$  nm (b) with light on/off cycles. The measured average results of PCD irradiated by all and visible wavelengths were 1600 and  $33 \mu\text{A}/\text{cm}^2$ , respectively.

dispersion was spin-coated on a dried composite film shown in Figure 4a, a higher coverage of  $\text{TiO}_2$  was achieved, as shown in Figure 4c, and the calcined film exhibited a honeycomb-structured  $\text{TiO}_2$  that displays interconnected spherical cavities (Figure 4d). The low-magnification SEM images of two films evidently showed an improved surface coverage of a honeycomb-structured  $\text{TiO}_2$  (Figure S3). The side-view SEM images at the bottom of Figures 4a and 4b show the as-transferred composite film and the resultant  $\text{TiO}_2$  film after calcination, respectively. The inset images show the top view of each film. The composite film exhibits 2-D hcp-structured PMMA  $\mu$ -spheres with  $\text{TiO}_2$  NPs at the interstices. The calcined film evidently exhibits a typical egg-plate structure from the sintered  $\text{TiO}_2$  NPs. An SEM image of highly covered  $\text{TiO}_2$  NPs without hcp structure disruption is shown at the bottom

of Figure 4c; furthermore, a subsequent thermal calcination resulted in a 2-D honeycomb structure, as shown in Figure 4d. Unlike the additional  $\text{TiO}_2$  coating as shown in Figure 4c, the spin coating of  $\text{TiO}_2$  NPs on the  $\mu$ -sphere-only monolayer seriously deteriorated the monolayer structure significantly because of low film integrity of the  $\mu$ -sphere-only film which was readily swept away during additional spin coating of  $\text{TiO}_2$  dispersion.

**Honeycomb-Structured  $\text{TiO}_2$  Thin Film for Photoelectrochemical (PEC) Water Splitting.** Crystalline  $\text{TiO}_2$  NPs are known to possess photocatalytic activity; thus, they can be utilized as antibacterial coating,<sup>22</sup> photoelectrodes for dye-sensitized solar cell,<sup>19,23,24</sup> and for PEC water splitting.<sup>25,26</sup> Recently, Zhang et al. fabricated a thin film of  $\text{TiO}_2$  nanotubes on Ti foil; moreover, by employing Au NPs on the film, they

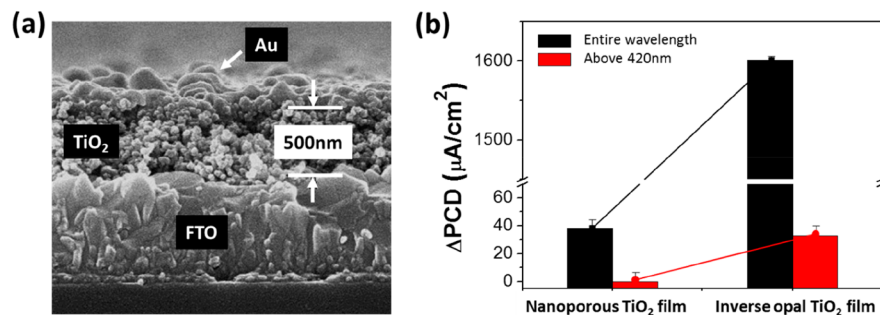


**Figure 7.** Comparison between conventional nanoporous TiO<sub>2</sub> thin film vs TiO<sub>2</sub> inverse opal thin film of the same thickness (~500 nm). (a) Cross-sectional SEM image of Degussa TiO<sub>2</sub> film on FTO. (b) Results of PCD measurement during PEC water splitting for comparison (PCD of Degussa TiO<sub>2</sub> film: 24 μA/cm<sup>2</sup> (black), 0.2 μA/cm<sup>2</sup> (red); PCD of TiO<sub>2</sub> inverse opal film: 1600 μA/cm<sup>2</sup> (black), 35 μA/cm<sup>2</sup> (red)).

obtained an improved PEC water-splitting performance at the visible wavelength.<sup>27</sup> Using the honeycomb-structured TiO<sub>2</sub> film fabricated in this study, we investigated PEC water splitting. The composite monolayer film of PMMA/TiO<sub>2</sub> on the air–water interface was transferred to a fluorine-doped tin oxide (FTO) and calcined to be utilized as a photoelectrode, as shown in Figure 5a. To enhance the quantum efficiency of TiO<sub>2</sub> at the visible wavelength, Au NPs of average size ~20 nm were photodeposited on the film<sup>27</sup> (Figure 5b). Figure 5c shows a honeycomb-structured TiO<sub>2</sub> film with Au NPs deposited on it. The film showed angle-dependent iridescent colors by 2-D diffraction over entire area, indicating the long-range ordered photonic crystal structure on FTO surface just as on glass substrate (Figure S4). As shown in Figure 5d, water splitting can occur under basic aqueous solution at the the TiO<sub>2</sub>/Au photoanode and counter electrode as well by PEC effects upon exposure to AM 1.5G light. PEC water splitting was performed in a custom-made quartz cell (Figure 5e).<sup>14</sup> To examine the PEC efficiency of the photoanode at the visible light wavelength, the measurements were performed with or without a long-pass filter (cutoff wavelength at 420 nm, Edmund Scientific).

As shown in Figure 6a, illuminating Xe light to a honeycomb-structured TiO<sub>2</sub> photoanode resulted in the generation of photocurrent by PEC reaction (~1600 μA/cm<sup>2</sup>) that stopped upon switching the light off. When the long-pass optical filter was used, the photocurrent generation was decreased to 35 μA/cm<sup>2</sup>, as shown in Figure 6b, which is a substantial PCD value under the visible light wavelength. Anatase TiO<sub>2</sub> is known to possess a bandgap of 3.0–3.2 eV, which corresponds to the photon energy of UV wavelength for photocatalytic activities.<sup>26,28</sup> When a TiO<sub>2</sub> photoanode without Au NPs was exposed to visible light, no current generation was observed. However, the photodeposition of 30 nm Au NPs on TiO<sub>2</sub> surface, as shown in Figure 5c, enabled an enhanced absorption of visible light because of the surface plasmon resonance effect<sup>27</sup> (Figure S5).

Theoretically, the photocurrent conversion efficiency (PCE) in PEC water splitting can be calculated using the *J–V* characteristic of the following equation:<sup>28</sup>

$$\text{PCE (\%)} = [J_p(1.23 \text{ V} - V_{\text{app}})/P_i] \times 100\% \quad (2)$$

where  $J_p$  denotes the current density upon exposure to light,  $V_{\text{app}}$  is the voltage at zero current, 1.23 V corresponds to the standard potential for water splitting, and  $P_i$  is the power density of exposed light. As shown in the *I–V* curve of Figure S6, electrochemical water splitting occurs above ~0.5 V vs Ag/

AgCl, and we applied 0.217 V in this study for PEC water splitting to minimize the electrochemical water-splitting effect. With a  $P_i$  of 100 mW/cm<sup>2</sup> and the obtained  $J_p$  of 1.6 mA/cm<sup>2</sup>, the calculated PCE is ~2%, which corresponds to ~200% improvement compared to a typical PCE value previously reported from a single cell composed of TiO<sub>2</sub> photoanodes.<sup>29</sup>

To compare the PEC water-splitting efficiency of the honeycomb-structured photoanode fabricated in this study, a nanoporous TiO<sub>2</sub> film of similar thickness to the IO film (~500 nm) was fabricated by coating a commercially available TiO<sub>2</sub> paste (Degussa P25 paste, Evonik) on FTO glass followed by the Au photodeposition process to produce an Au-coated TiO<sub>2</sub> film structure as shown in Figure 7a.

Exposing the same intensity of light with or without the long-pass filter resulted in PCDs of 0.2 and 24 μA/cm<sup>2</sup>, and a comparison indicates that the PCDs obtained from the honeycomb-structured TiO<sub>2</sub> film are 175 and 67 times larger than those with nanoporous TiO<sub>2</sub> films, respectively, as shown in Figure 7b. Even though there is much less TiO<sub>2</sub> coated in the honeycomb-shaped TiO<sub>2</sub> film with hcp pore structure compared to a nanoporous TiO<sub>2</sub> film with the same thickness and area, it is worthwhile to note that the honeycomb structured film showed substantially higher PCDs under the both visible and the UV light. Such results can be attributed to the highly ordered pore structure which exposes much larger surface area to the illumination of light, thus enabling an improved PEC water-splitting reaction.

#### 4. CONCLUSION

In this study, a large-area fabrication of 2-D PMMA/TiO<sub>2</sub> composite photonic crystal monolayer was demonstrated successfully. Monodisperse 31 nm TiO<sub>2</sub> NPs and 564 nm PMMA  $\mu$ -spheres with negative surface charge were synthesized, and their binary aqueous dispersions formed a composite monolayer with long-range ordered hexagonal packing structure on the air–water interface. A closer packing density compared to that of a PMMA-only monolayer was attributed to an entropic depletion interaction between the  $\mu$ -spheres provided by TiO<sub>2</sub> NPs at the vicinity of the  $\mu$ -sphere surfaces. An additional spin coating of TiO<sub>2</sub> NPs on a transferred composite monolayer on a glass substrate and subsequent calcination formed an unprecedented honeycomb-structured TiO<sub>2</sub> inverse opal film. Such a film could be fabricated onto FTO glass, which was tested as a photoelectrode for PEC water splitting. By measuring photocurrent densities upon the exposure of UV light of either the entire wavelength range or that above 420 nm, it was confirmed that the honeycomb-

structured TiO<sub>2</sub> thin film exhibited 67 times enhancement in PCD compared to a conventional photoanode with nanoporous TiO<sub>2</sub>, which was enabled by a large surface area from the highly ordered 2-D porous structure of the film.

## ■ ASSOCIATED CONTENT

### 📄 Supporting Information

The Supporting Information is available free of charge at <https://pubs.acs.org/doi/10.1021/acsnm.9b01789>.

Figures S1–S6 (PDF)

## ■ AUTHOR INFORMATION

### Corresponding Author

\*(W.L.) E-mail [wonmokee@sejong.ac.kr](mailto:wonmokee@sejong.ac.kr).

### ORCID

Wonmok Lee: 0000-0001-6757-885X

### Notes

The authors declare no competing financial interest.

## ■ ACKNOWLEDGMENTS

This study was financially supported by the Basic Science Research Program through the National Research Foundation of Korea (NRF), which was funded by the Ministry of Science, ICT, and Future Planning (Grant No. NRF-2019R1A2C1010088).

## ■ REFERENCES

- (1) van Dommelen, R.; Fanzio, P.; Sasso, L. Surface self-assembly of colloidal crystals for micro- and nano-patterning. *Adv. Colloid Interface Sci.* **2018**, *251*, 97–114.
- (2) Ilinykh, V. A.; Matyushkin, L. B. Sol-gel fabrication of one-dimensional photonic crystals with predicted transmission spectra. *J. Phys.: Conf. Ser.* **2016**, *741*, 012008.
- (3) Zhang, J.; Wang, L.; Lamont, D. N.; Velankar, S. S.; Asher, S. A. Fabrication of Large-Area Two-Dimensional Colloidal Crystals. *Angew. Chem., Int. Ed.* **2012**, *51*, 6117–6120.
- (4) Takahashi, S.; Suzuki, K.; Okano, M.; Imada, M.; Nakamori, T.; Ota, Y.; Ishizaki, K.; Noda, S. Direct creation of three-dimensional photonic crystals by a top-down approach. *Nat. Mater.* **2009**, *8* (9), 721–725.
- (5) Cai, Z.; Smith, N. L.; Zhang, J. T.; Asher, S. A. Two-dimensional photonic crystal chemical and biomolecular sensors. *Anal. Chem.* **2015**, *87* (10), 5013–5025.
- (6) Arsenault, A. C.; Puzzo, D. P.; Ghossoub, A.; Manners, I.; Ozin, G. A. Development of photonic crystal composites for display applications. *J. Soc. Inf. Dispersion* **2007**, *15* (12), 1095–1098.
- (7) Wang, W.; Qi, L. Light Management with Patterned Micro- and Nanostructure Arrays for Photocatalysis, Photovoltaics, and Optoelectronic and Optical Devices. *Adv. Funct. Mater.* **2019**, *29* (25), 1807275.
- (8) Mihi, A.; Ocaña, M.; Míguez, H. Oriented colloidal-crystal thin films by spin-coating microspheres dispersed in volatile media. *Adv. Mater.* **2006**, *18*, 2244–2249.
- (9) Lotito, V.; Zambelli, T. Self-Assembly of Single-Sized and Binary Colloidal Particles at Air/Water Interface by Surface Confinement and Water Discharge. *Langmuir* **2016**, *32* (37), 9582–9590.
- (10) Vogel, N.; de Viguier, L.; Jonas, U.; Weiss, C. K.; Landfester, K. Wafer-Scale Fabrication of Ordered Binary Colloidal Monolayers with Adjustable Stoichiometries. *Adv. Funct. Mater.* **2011**, *21*, 3064–3073.
- (11) Dai, Z.; Li, Y.; Duan, G.; Jia, L.; Cai, W. Phase Diagram, Design of Monolayer Binary Colloidal Crystals, and Their Fabrication Based on Ethanol-Assisted Self-Assembly at the Air/Water Interface. *ACS Nano* **2012**, *6* (8), 6706–6716.
- (12) Egen, M.; Zentel, R. Tuning the Properties of Photonic Films from Polymer Beads by Chemistry. *Chem. Mater.* **2002**, *14* (5), 2176–2183.
- (13) Seo, Y.; Lee, H.; Kim, K.; Lee, W. Transparent Thin Films of Anatase Titania Nanoparticles with High Refractive Indices Prepared by Wet Coating Process. *Mol. Cryst. Liq. Cryst.* **2010**, *520*, 201–208.
- (14) Distler, D.; Kanig, G. Fine structure of polymers of aqueous structure. *Colloid Polym. Sci.* **1978**, *256* (11), 1052–1060.
- (15) Moon, G. D.; Lee, T. I.; Kim, B.; Chae, G.; Kim, J.; Kim, S.; Myoung, J.-M.; Jeong, U. Assembled Monolayers of Hydrophilic Particles on Water Surfaces. *ACS Nano* **2011**, *5* (11), 8600–8612.
- (16) Scriven, L. E.; Sternling, C. V. The Marangoni Effect. *Nature* **1960**, *187*, 186–188.
- (17) Tohver, V.; Smay, J. E.; Braem, A.; Braun, P. V.; Lewis, J. A. Nanoparticle halos: A new colloid stabilization mechanism. *Proc. Natl. Acad. Sci. U. S. A.* **2001**, *98* (16), 8950–8954.
- (18) Lee, W.; Chan, A.; Bevan, M. A.; Lewis, J. A.; Braun, P. V. Nanoparticle-Mediated Epitaxial Assembly of Colloidal Crystals on Patterned Substrates. *Langmuir* **2004**, *20*, 5262–5270.
- (19) Seo, Y. G.; Kim, M. A.; Lee, H.; Lee, W. Solution processed thin films of non-aggregated TiO<sub>2</sub> nanoparticles prepared by mild solvothermal treatment. *Sol. Energy Mater. Sol. Cells* **2011**, *95*, 332–335.
- (20) Ohara, P. C.; Leff, D. V.; Heath, J. R.; Gelbart, W. M. Crystallization of Opals from Polydisperse Nanoparticles. *Phys. Rev. Lett.* **1995**, *75*, 3466–3469.
- (21) Bishop, K. J. M.; Wilmer, C. E.; Soh, S.; Grzybowski, B. A. Nanoscale Forces and Their Uses in Self-Assembly. *Small* **2009**, *5*, 1600–1630.
- (22) Burnside, S. D.; Shklover, V.; Barbé, C.; Comte, P.; Arendse, F.; Brooks, K.; Grätzel, M. Self-Organization of TiO<sub>2</sub> Nanoparticles in Thin Films. *Chem. Mater.* **1998**, *10* (9), 2419–2425.
- (23) Kay, A.; Grätzel, M. Low cost photovoltaic modules based on dye sensitized nanocrystalline titanium dioxide and carbon powder. *Sol. Energy Mater. Sol. Cells* **1996**, *44*, 99–117.
- (24) Kwak, E.; Lee, W.; Park, N.; Kim, J.; Lee, H. Compact Inverse-Opal Electrode Using Non-Aggregated TiO<sub>2</sub> Nanoparticles for Dye-Sensitized Solar Cells. *Adv. Funct. Mater.* **2009**, *19*, 1093–1099.
- (25) Wang, C.; Deng, Z.-X.; Li, Y. The Synthesis of Nanocrystalline Anatase and Rutile Titania in Mixed Organic Media. *Inorg. Chem.* **2001**, *40* (20), 5210–5214.
- (26) Linsebigler, A. L.; Lu, G.; Yates, J. T. Photocatalysis on TiO<sub>2</sub> Surfaces: Principles, Mechanisms, and Selected Results. *Chem. Rev.* **1995**, *95* (3), 735–758.
- (27) Zhang, Z.; Zhang, L.; Hedhili, M. N.; Zhang, H.; Wang, P. Plasmonic gold nanocrystals coupled with photonic crystal seamlessly on TiO<sub>2</sub> nanotube photoelectrodes for efficient visible light photoelectrochemical water splitting. *Nano Lett.* **2013**, *13*, 14–20.
- (28) Chen, Z.; Dinh, H.; Miller, E. *Photoelectrochemical Water Splitting: Standards, Experimental Methods, and Protocols*; Springer-Verlag: New York, 2013; p 10.
- (29) Rathakrishnan, E. The 2nd International Symposium on Recent advances in Experimental Fluid Mechanics. *J. Visualization* **2009**, *12* (1), 81–86.